

Bulk photovoltaic effect in ferroelectric and antiferroelectric phases of antimony sulphoiodide investigated by means of ab-initio simulations

Giuseppe Cuono¹, Andrea Droghetti², Silvia Picozzi^{3,1}

¹Consiglio Nazionale delle Ricerche (CNR-SPIN), Unitá di Ricerca presso Terzi c/o
Universitá “G. D’Annunzio”, 66100 Chieti, Italy.
E-mail: giuseppe.cuono@spin.cnr.it

²Department of Molecular Sciences and Nanosystems, Ca’ Foscari University of Venice,
via Torino 155, 30170, Venice-Mestre, Italy.
E-mail: andrea.droghetti@unive.it

³Department of Materials Science, University Milan-Bicocca, 20125 Milan, Italy.
E-mail: silvia.picozzi@unimib.it

Abstract

First-principles calculations are employed to study the ferroelectric properties and the bulk photovoltaic effect (BPVE) of antimony sulfur iodide (SbSI). The BPVE enables direct sunlight-to-electricity conversion in homogeneous materials and, in ferroelectric compounds, can be tuned via an electric field controlling the polarization. However, most ferroelectrics are oxides with large band gaps exceeding visible light energy, limiting their photovoltaic performance. Featuring a visible-range band gap, SbSI instead combines remarkable photovoltaic capabilities with a spin-textured band structure, coupling charge and spin degrees of freedom. The calculations predict ferroelectric and antiferroelectric phases with comparable band gaps but distinct Rashba-Dresselhaus and Weyl-like spin textures relevant for spintronics. The BPVE is driven by the linear and circular photogalvanic effects, exhibiting large photoconductivities under visible light. Furthermore, it can serve to identify the phase of the material, with the circular photogalvanic effect which also reflects spin-texture changes. With its multifunctional properties, SbSI emerges as a promising material candidate for efficient solar energy conversion and advanced electronics, with potential applications extending to spintronics.

1 Introduction

The bulk photovoltaic effect (BPVE) converts solar power into electrical power within homogeneous systems [1, 2, 3, 4]. Unlike the conventional photovoltaic effect, which requires a built-in potential at material interfaces (e.g., p-n junctions) to separate the photogenerated charge carriers, the BPVE allows for simpler device structures where the entire bulk material contributes to the photocurrent generation. Furthermore, the BPVE can result in above-band-gap open circuits voltages, as carriers are collected before they

thermalize, thereby surpassing the Shockley–Queisser limit which constrains conventional solar cells [5, 6].

The primary contributions to the BPVE are the shift and injection currents [7, 4, 8, 9], both second-order responses to the incident light field. The shift current [10] is an interband phenomenon, which can be interpreted as a real-space displacement of electrons upon light excitation [4, 11, 12]. In contrast, the injection current arises from asymmetries in the velocity distribution of excited carriers [1] due to non-reciprocal band structures [13] or processes like asymmetric carriers photoexcitation, recombination, and momentum relaxation [14]. Recently, either the shift current, the injection current, or both have been investigated experimentally [15, 16, 17, 18, 19, 20, 21, 22, 23, 24] as well as theoretically [25, 26, 27, 28] across numerous systems.

Within a single-particle framework (i.e., considering only band structure effects), symmetry considerations allow these currents to be further classified based on whether they are driven by linearly or circularly polarized light. Specifically, in non-magnetic materials where time-reversal symmetry is preserved, linearly polarized light induces the shift current (linear photogalvanic effect), whereas circularly polarized light generates the injection current (circular photogalvanic effect), whose direction depends on the light’s helicity [9, 12]. The linear photogalvanic effect occurs in noncentrosymmetric materials, and more precisely, in materials with piezoelectric point groups, while the circular photogalvanic effect is seen in a further subset of these systems, known as gyrotropic materials (out of the 32 point groups, 21 are noncentrosymmetric; among these, 20 point groups exhibit piezoelectric properties, and 18 of those are also gyrotropic).

Among the materials exhibiting both photogalvanic effects, ferroelectric (FE) compounds with spontaneous electrical polarization have attracted significant interest [1, 29, 30, 31, 32, 33], as the photocurrent direction can be controlled by reversing the polarization via an electric field. Despite that, the most studied FE materials, such as the perovskite oxides LiNbO_3 , BaTiO_3 [29, 30], BiFeO_3 [31] and PbTiO_3 [30] have large band gaps greater than 3 eV, limiting their ability to capture sunlight to the ultraviolet (UV) range, which accounts for only about 3.5% of the total solar spectrum. For efficient photoconversion, ideal materials should possess narrower band gaps, strong absorption in the visible spectrum [34], along with long carrier lifetimes and diffusion length [35].

As an alternative to FE oxide materials, group-IV monochalcogenide monolayers, such as GeS, GeSe, SnS, and SnSe, have been proposed due to their smaller band gaps and high carrier mobilities [36]. While these monochalcogenides are centrosymmetric in their bulk form, they lack inversion symmetry in their monolayer configurations, which allows for the emergence of spontaneous electrical polarization and large shift [36] and injection currents [37] under visible light. Moreover, first-principles calculations predict that these currents are enhanced owing to the reduced dimensionality of the materials [36]. Despite that, experimental measurements on non-centrosymmetric layer-stacked SnS have reported much lower photocurrents than expected [38, 39]. This discrepancy has been attributed to the presence of multiple ferroelectric domains with opposing spontaneous polarizations in the samples, which reduces the overall shift current by averaging out the individual domain contributions [38].

Another promising alternative to oxide materials is antimony sulfoiodide (SbSI), which has a visible-range band gap [40], equal to approximately 1.9 eV. SbSI belongs to the class of multifunctional materials known as FE Rashba-Dresselhaus semiconductors [41, 42]. In these materials, strong spin-orbit coupling (SOC) is combined with ferroelectricity resulting in spin-textured electronic bands characterized by a large Rashba-Dresselhaus

spin splitting that can be controlled by applying an electric field [42]. This effect can find applications in novel device concepts for spintronic applications [43]. Furthermore, the Rashba-Dresselhaus spin-texture is also predicted to lead to long photocarriers lifetimes [44, 45]. Consequently, FE Rashba-Dresselhaus semiconductors possess all the essential characteristics for efficient and tuneable photoconversion, which, moreover, can potentially be further integrated with electronic and spin transport functionalities.

The discovery of ferroelectricity in SbSI dates back to 1962, with a reported spontaneous polarization of about $25 \mu\text{C}/\text{cm}^2$ at 0°C [46]. It was later found that SbSI also exhibits an antiferroelectric (AFE) phase in the temperature range $295 \text{K} < T < 410 \text{K}$, above which the material transitions to the paraelectric phase. In the FE phase, SbSI exhibits high photoconductivity [47] and nonlinear optical behavior [48]. Moreover, the shift current has been experimentally measured [49, 50, 51], yielding an extrapolated photoconductivity of $\sim 10 \mu\text{A}/\text{V}^2$, which is one of the largest reported values for a FE semiconductor. In contrast, the AFE phase, and its optical and photoconductive properties, have been far less studied, despite the AFE phase occurring near room temperature.

In this paper, we use first-principles calculations based on Density Functional Theory (DFT) to fill the knowledge gap regarding the different phases of SbSI, providing an accurate description of the BPVE. Specifically, we begin by comparing the FE and AFE structural and electronic properties, predicting that the phase transition also leads to a drastic modification of the band structure spin-texture, which could be of potential interest for spintronics. We then proceed with a detailed analysis of the BPVE, accurately estimating the shift and circular injection photoconductivities, and demonstrating that the latter is also related to the band structure spin-texture. Two main findings emerge from our study. First, the photocurrent can reach very large peak values within the visible energy range in both the FE and AFE phases, confirming the potential of the material for photovoltaic applications. Second, the direction of both shift and circular photocurrents changes as the system transitions from the FE to the AFE phase, due to the change in the crystal space group. Given that the FE-AFE phase transition occurs near room temperature and the photoresponses are experimentally accessible, we then propose that the BPVE can serve as a reliable probe of the phase transition. Moreover, we also show that measuring circular injection currents can track the material's evolution from a Rashba-Dresselhaus spin character in the FE phase to a Dresselhaus-Weyl character in the AFE phase, revealing the intricate coupling between structural and spintronic properties.

The paper is organized as follows. The computational details are reported in section 2. The results are presented in section 3: we describe the structural properties in subsection 3.1, estimate the macroscopic polarization in subsection 3.2, analyze the band structure in subsection 3.3, and the photoconductivities in subsection 3.4. Finally, in section 4, we summarize our conclusions.

2 Computational details

DFT calculations are performed by using the projector-augmented wave method, as implemented in the VASP package [52, 53, 54]. The Perdew-Burke-Erzenhof (PBE) [55] generalized gradient approximation (GGA) is used for the exchange-correlation functional in most of our simulations, while the Heyd-Scuseria-Ernzerhof 2006 (HSE06) hybrid density functional approach [56, 57] is employed to correct for the short-coming of the GGA

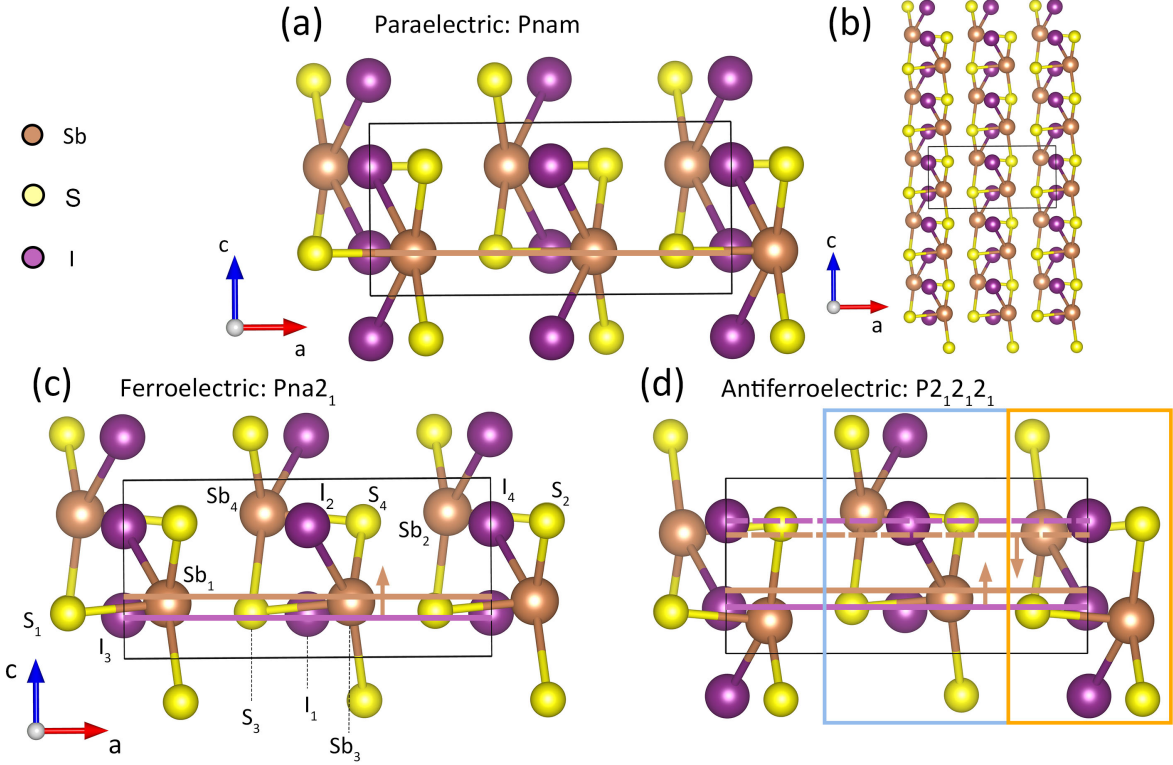


Figure 1: Crystal structure of SbSI in the PE (space group Pnam), FE (space group Pna2₁) and AFE (space group P2₁2₁2₁) phases. (a) In the PE configuration, the Sb, S and I ions occupy the same position along the c axis (see brown line). The polarization is zero. (b) The system is composed of zig-zag chains propagating along the c axis. (c) In the FE phase, the Sb sub-lattice is shifted with respect to the anions sub-lattice along the c axis and FE polarization appears. In this configuration the cations are shifted in the same direction in both chains, as indicated by the brown arrow. The cation and anion sub-lattices have different z coordinates (see brown and purple lines). (d) In the AFE phase, the cations of one chain shift in one direction, while the cations of the other chain shift in the opposite direction, as indicated by brown arrows. The blue and orange rectangles highlight the two different chains. The solid brown and purple lines indicate the positions along c of the cations and anions in one chain, while the dashed brown and purple lines in the other chain. In the AFE configuration the polarization is zero; however, in both the FE and AFE phases the inversion symmetry is broken.

in describing the energetics of the system and the size of the band gap. The van der Waals (vdW) dispersion energy is included in the structural relaxation using the DFT-D3 method of Grimme *et al.* [58]. The plane-wave energy cutoff is set to 400 eV. The atomic positions are optimized until the residual forces are smaller than 0.01 eV Å⁻¹. The calculation of the macroscopic electric polarization is performed within the modern theory of polarization through the Berry phase method [59]. For the geometry optimizations, the Brillouin zone is sampled with 4 × 4 × 8 Monkhorst-Pack k -grid centered at the Γ point. This grid is refined to 8 × 8 × 12 in the self-consistent calculations at the optimized geometries, since the photoresponses are highly sensitive to the used k -mesh.

The linear and circular photogalvanic effects are described in terms of their photoconductivity tensors, using the approach developed by Azpiroz *et al.* [11] and Puente-Uriona

et al. [12]. This approach is based on interpolation of the DFT band structure using maximally-localized Wannier functions [60, 61], as implemented in the WANNIER90 package [62]. The s and p -orbitals of Sb, S, and I ions are considered, resulting in a total of 96 bands when spin-orbit coupling (SOC) is included. For bulk systems, a $100 \times 100 \times 100$ k -grid is used together with the adaptive broadening scheme described in Ref. [63] to cope with the Dirac delta functions. For the single-chain system, a $1 \times 1 \times 100$ k -grid is employed, with a fixed broadening of 0.02 eV to better handle the van Hove singularities, following the method of Azpiroz *et al.* [11]. With these k -grids, the photoconductivities are well converged, and no significant differences in the results are observed when the grid density is further increased. SOC is included in all calculations of the band structure and photocurrents, while it is neglected in the geometry optimizations, on which SOC is expected to have no effect.

3 Results and discussion

3.1 Structural properties

In the paraelectric (PE) phase, SbSI has an orthorhombic crystal structure, which belongs to the centrosymmetric space group Pnam [64], with four formula units (i.e., 12 atoms) in the primitive unit cell [Fig. 1(a)]. The structure consists of zigzag chains propagating along the c -axis (assumed parallel to the z Cartesian axis) which are weakly bonded by van der Waals interactions [Fig. 1(b)]. The primitive unit cell contains two zigzag chains. Within each chain, the atoms are grouped in parallel layers in the xy plane, and the bonds are characterized by a high degree of covalency. However, for a simplified understanding, one can describe a chain in terms of ionic bonds, assigning oxidation states of Sb^{3+} , S^{2-} and I^{1-} to the atoms.

In the PE phase, both cations and anions are placed at the same z coordinate. In contrast, in the FE phase, a cooperative displacement of Sb atoms results in a shift of the cation sub-lattice along the c -axis relative to the anion I and S sub-lattices, as shown in Fig. 1 (c). The Sb ions play a primary role by displacing more than the other atoms with respect to their centrosymmetric positions, breaking inversion symmetry and creating a polarization along the c -axis [65]. This behavior can be attributed to the presence of a Sb^{3+} lone pair, extending in the empty region between the chains and tilting along the c axis in the FE phase so to minimize the Coulomb repulsion with the other bonding electrons [65]. The crystal structure in the FE phase remains orthorhombic as in the PE phase, but the space group changes to Pna2₁.

The crystal structure of AFE phase has not been studied in detail to date. Here, we propose a configuration, where the cations in one chain shift in one direction along the c -axis as in FE phase and the cations in adjacent chains move in the opposite direction [Fig. 1(d)]. As a result, each chain exhibits a polarization, but the polarizations of neighboring chains are oriented in opposite (antiparallel) directions, leading to a net zero polarization for the overall system. The crystal structure of this AFE phase is P2₁2₁2₁.

The FE distortion can not be reproduced by means of DFT within the standard GGA functional, because the structural optimization tends to converge to the PE structure, as already reported in previous studies [65]. To overcome this problem, we perform ionic relaxations using the hybrid functional HSE06 [57], by also taking into account the Van der Waals interaction among the chains. The HSE06 functional is known to effectively capture the delicate balance between electronic properties and lattice distortions [66, 67].

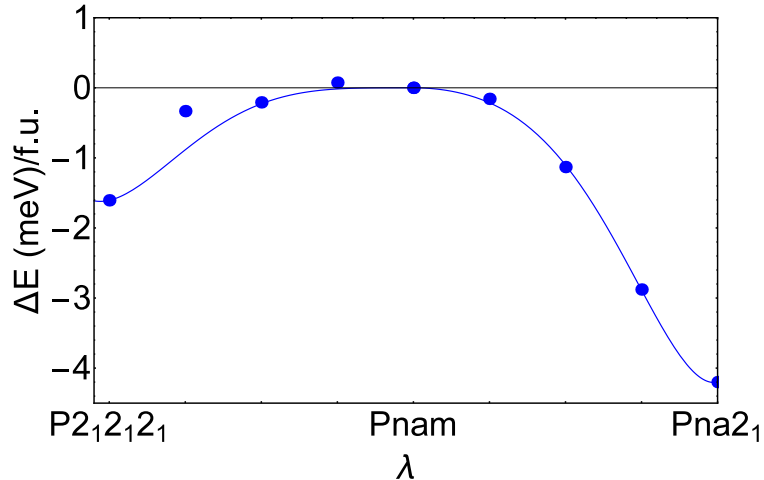


Figure 2: Energy path from the AFE ($P2_12_12_1$) to the FE phase ($Pna2_1$), through the PE configuration ($Pnam$), built by means of linear interpolation of lattice parameters and coordinates. The curve follows Landau theory and represents an expansion of the energy difference in even powers of the generalized parameter λ , up to the sixth order.

In our HSE calculations, the FE configuration is found to be lower in energy than the PE and AFE configurations by 4.20 meV and 2.59 meV per formula unit, respectively; in other words, the AFE configuration is the second lowest in energy. Therefore, our results reproduce the stability ordering of the three phases observed in experiments. The optimized lattice parameters and atomic positions in the PE, FE and AFE phases are reported in detail in the Supporting Information (SI). The obtained values are in good agreement with experiments. For example, in the FE phase, our optimized lattice parameters are $a=8.56$ Å, $b=10.10$ Å and $c=4.16$ Å, while the experimental ones are respectively 8.49 Å, 10.10 Å and 4.16 Å [68]. The lattice parameters only slightly differ in the AFE and FE phases. Notably, in both these phases, the chains tend to elongate along the c -axis with respect to the PE geometry. In fact, we find that the c lattice parameter increases from 4.10 Å in the PE phase to 4.16 Å, and 4.17 Å in the FE and AFE phases, respectively. This points to a “strain-polarization” coupling: while polarization develops, the c -axis elongates, in close similarity to what happens for standard ferroelectrics, such as $P4mm$ $BaTiO_3$. In the PE phase, the atom labeled Sb_3 in Fig. 1(c) is positioned at the same z coordinate as the I_1 and S_3 atoms. In contrast, in both the FE and AFE phases, Sb_3 is displaced along the c axis relative to I_1 and S_3 by $\Delta z_{Sb_3-I_1} = 0.29$ Å and $\Delta z_{Sb_3-S_3} = 0.21$ Å. These values, which quantify the polar distortion, are slightly overestimated but in reasonable agreement with the experimental values for the FE phase, which are 0.21 Å and 0.17 Å [69]. This demonstrates the good performance of HSE calculations in predicting the FE structure of the material.

3.2 Electrical polarization

The macroscopic electrical polarization, \mathbf{P} , is calculated within the modern theory of polarization through the Berry phase method [59]. We build an adiabatic path from the optimized PE to FE and AFE structures by linearly interpolating both lattice parameters and atomic positions, labeled by a generalized coordinate λ , as depicted in Fig. 2. The parameter runs from -1 (AFE structure with space group $P2_12_12_1$) through 0 (PE

	Z_{xx}^*	Z_{xy}^*	Z_{xz}^*	Z_{yx}^*	Z_{yy}^*	Z_{yz}^*	Z_{zx}^*	Z_{zy}^*	Z_{zz}^*
Sb	1.89	0.04	0	0.94	3.67	0	0	0	6.84
S	-1.09	-0.07	0	-0.88	-1.76	0	0	0	-3.83
I	-0.80	-0.43	0	-0.81	-1.90	0	0	0	-3.01

Table 1: BEC in the PE phase calculated within the GGA.

structure with Pnam space group), and up to 1 (FE structure with Pna2₁ space group). The resulting energy profile shows a characteristic (asymmetric) double-well shape, with an energy barrier of 4.20 meV per f.u. between the FE and PE phase, and a lower energy barrier of 2.59 meV between the AFE and the PE phase, as anticipated in the previous subsection.

The macroscopic polarization in the FE phase lies along the c -axis, as expected from symmetry, with a calculated magnitude of $P \simeq 31$ (30) $\mu\text{C}/\text{cm}^2$ with the HSE06 (GGA) functional, in good agreement with experimental results [46] and previous DFT calculations [65]. Notably, for fixed structures, the polarization value is very similar when using either the GGA or HSE functional. Therefore, even though the GGA fails in estimating the correct energetics of the system and in the geometry optimization of the FE state, it performs well for the ferroelectric properties.

The macroscopic polarization in the AFE phase is zero. However, we can estimate the polarization of a single chain approximately by computing the tensor of the Born effective (or dynamical) charges (BEC) [70, 71], Z_{ab}^* with $a, b = x, y, z$. The contribution of each atom to polarization can be defined as the product of the BEC and the displacements of the atom in all three Cartesian directions relative to their positions in the PE configuration [72]. The polarization of a single chain is then obtained by summing over the contributions of all the atoms in the chain. In Table 1, we provide the components of the BEC tensor calculated for the PE phase, computed using the GGA functional. We also note that there are no significant differences between the BEC values obtained with the GGA and HSE functionals.

For consistency, we use the BEC values from the PE phase to calculate the polarization in both the FE and AFE configurations. The BEC tensor for the FE phase is reported in the SI. As expected, the BEC components are positive for the cations and negative for the anions. The BEC values are large, deviating from the nominal ionic charges (namely, +3 for Sb, -1 for I, and -2 for S) indicating substantial charge redistribution across the bonds compared to an ideal ionic model, in particular along the z direction. The highest BEC values are obtained for the Sb atoms, which play the crucial role of most "active sites" in the material's polarization, as discussed earlier.

The polarization in the FE phase, calculated using the BEC method, is $\simeq 30 \mu\text{C}/\text{cm}^2$, a value very close to the one obtained through the Berry phase approach, confirming the reliability of the approximation. In the AFE phase, the polarization of a single chain is $\simeq 30 \mu\text{C}/\text{cm}^2$, indicating that the FE and AFE phases exhibit similar polarization values along the c -axis, despite the overall macroscopic polarization of the latter phase being zero due to the antiparallel alignment of adjacent chains.

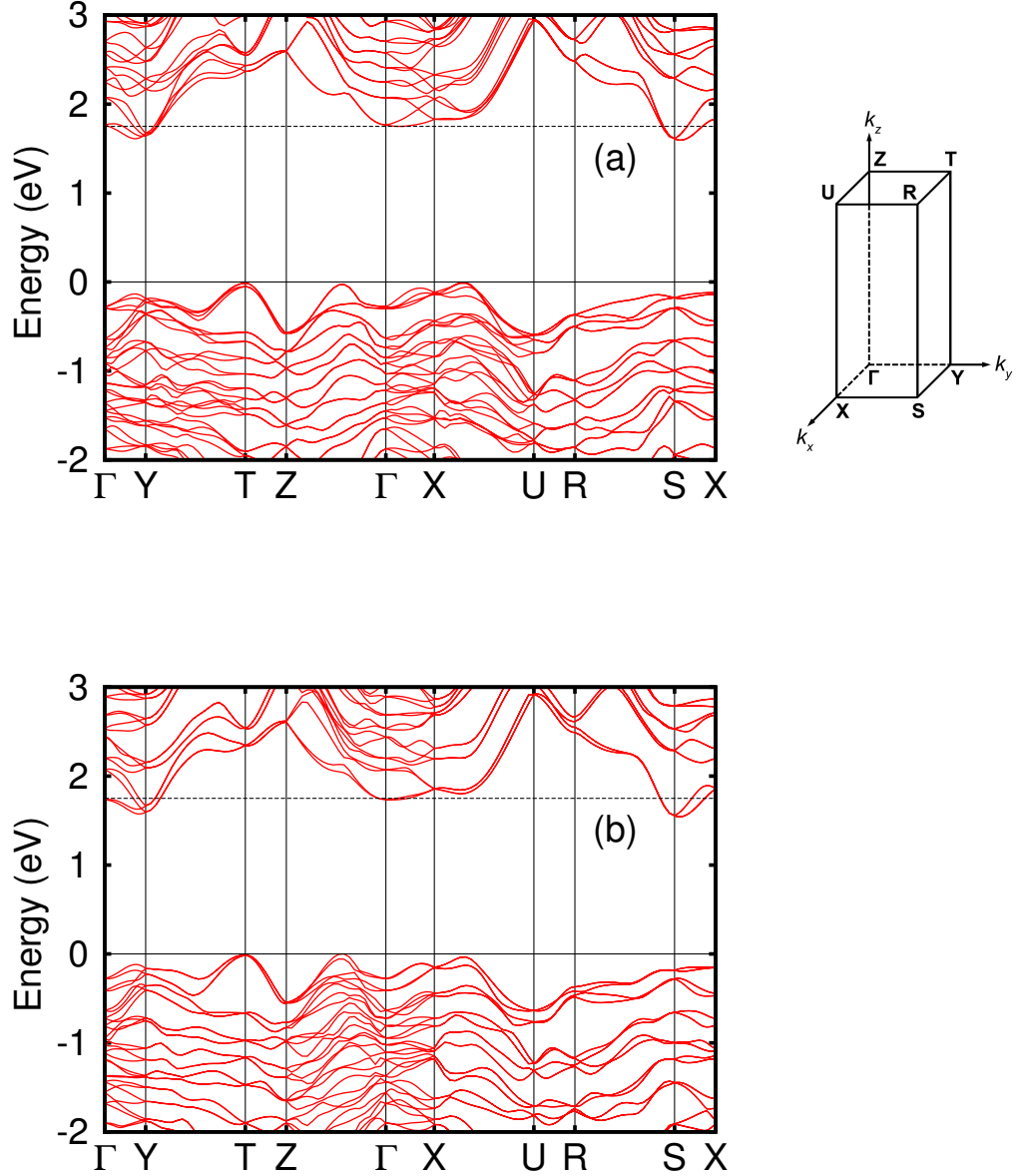


Figure 3: DFT band structure for the FE phase (a) and for the AFE phase (b). The inset displays the Brillouin zone. The Fermi energy is set at 0 eV. The horizontal dashed line indicates the energy surface where the spin textures are calculated.

3.3 Band structure

The band structures of the FE and AFE phases, calculated within the GGA and including SOC, are displayed in Fig. S2(a) and (b), respectively. The results for the FE phase are consistent with previous studies [65, 32, 73]. The bands are quite wide along paths in the Brillouin zone parallel to the k_z direction (e.g., Z- Γ line or X-U), while they narrow along the in-plane directions (e.g., Γ -X line), reflecting the weak inter-chain hybridization. Compared to the GGA, HSE gives a rigid upward shift of the conduction bands without significantly modifying the main electronic features and the overall band dispersion. The HSE band structure is shown in the SI.

The band gap in the FE phase is indirect [see Fig. S2(a)]. The minimum of the

conduction band is at the S point of the Brillouin zone, while three maxima of the valence band, with similar energies, are located at the T point and along the X-U and Z- Γ line. The size of this indirect gap is 1.61 eV in the GGA, and increases to 2.29 eV when using HSE. A direct gap exist along the Γ -Y line and is equal to 1.75 eV in the GGA and 2.59 eV in HSE. All these gap values fall within the visible energy range of the electromagnetic spectrum, confirming that SbSI is potentially suitable for photovoltaic applications.

Compared to the experimental value of 1.88 eV [40], the band gap of the FE phase is only slightly underestimated in the GGA, and conversely, drastically overestimated by HSE. However, it is important to note that the experimental band gap is determined by excitonic effects, which reduce the optical gap with respect to the single-particle one. These effects are not accounted for in the DFT band structure. Thus, the apparent agreement between the GGA result and experimental value may be due to a fortuitous compensation between the well-known band gap problem of DFT and the omission of exciton binding energies in the calculations.

In the AFE phase [see Fig. S2(b)], the size of the band gap, as well as the positions of the valence band maximum and conduction band minimum, remain similar to those in the FE phase. Hence, we expect light adsorption to occur in the same energy range, making the AFE phase equally suitable for exploiting the BPVE.

The main differences between the FE and AFE phases are observed in some bands that are degenerate in one phase but split by the SOC in the other. This is a direct consequence of the change in the crystal space group during the phase transition. A particularly insightful analysis can be made around the Γ point; despite the intricate band structure, one can resort to an effective linear spin-momentum Hamiltonian for a qualitative understanding. In the FE phase, the point group symmetry at Γ is C_{2v} . Thus, the effective SOC terms acquire the form $\alpha_{xy}k_x\tau_y$ and $\alpha_{yx}k_y\tau_x$, where τ_x and τ_y are the Pauli matrices, and α_{xy} and α_{yx} are coupling parameters representing the non-zero components of a rank-two spin-momentum coupling pseudotensor [74]. These effective SOC terms can be rewritten in the standard Rashba and Dresselhaus forms by performing an appropriate unitary transformation and lead to a characteristic in-plane spin-texture [65]. Because of this peculiar feature, SbSI is referred to as a FE Rashba-Dresselhaus semiconductor.

In contrast, in the AFE phase, the point group symmetry at Γ is D_2 , leading to a different effective Hamiltonian. Specifically, the SOC terms now take the form $\alpha_{xx}k_x\tau_x$, $\alpha_{yy}k_y\tau_y$, and $\alpha_{zz}k_z\tau_z$, where α_{xx} , α_{yy} , α_{zz} are the non-zero components of a spin-momentum coupling pseudotensor consistent with the D_2 symmetry. These SOC terms give rise to a Dresselhaus-Weyl spin-texture [75]. The effect of the $\alpha_{zz}k_z\tau_z$ term is particularly evident in the band structure, where bands along the Z- Γ direction, which are two-fold degenerate in the FE phase, become spin-split in the AFE phase.

The spin-textures obtained from the DFT calculations are shown in Fig. 4, with the blue arrows representing the directions of expectation values of Pauli spin-matrices. In particular, panel (a) shows the plot in the $k_z = 0$ plane at the constant energy surface $E - E_{\text{VBM}} = 1.75$ eV above the valence band maximum (VBM) (see the horizontal dashed line in Fig. S2) for the FE phase, while panel (b) shows the plot in the $k_x = 0$ plane at the same constant energy surface for the AFE phase. Panels (c) and (d) are zoomed-in views of panels (a) and (b) around the Γ point. In panel (c), we clearly observe the characteristic Rashba-Dresselhaus spin-texture, with the Dresselhaus component dominating, consistent with previous reports for the FE phase [65]. In contrast, panel (d) reveals that

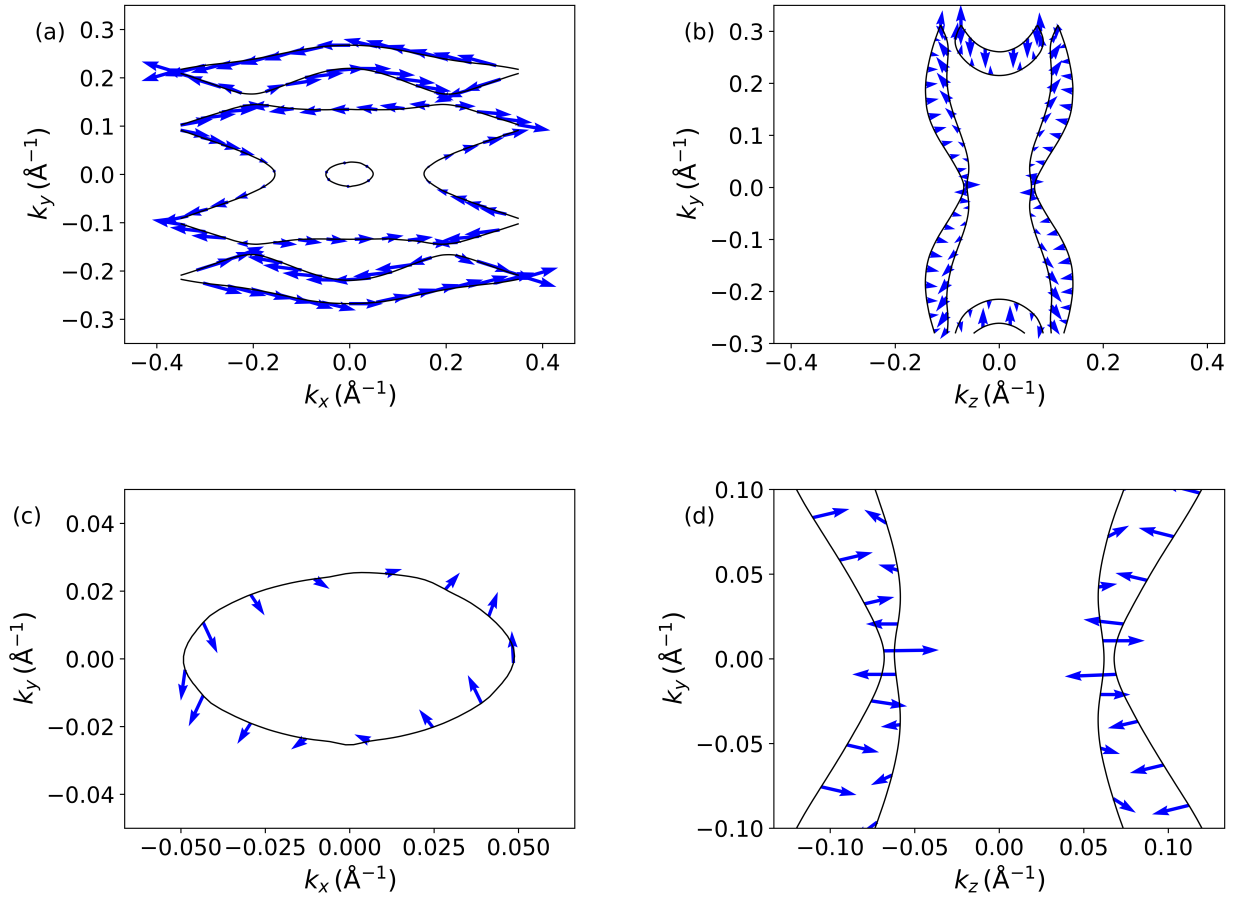


Figure 4: Spin textures calculated by DFT. (a) plot in the $k_z = 0$ plane at the constant energy surface $E - E_{\text{VBM}} = 1.75$ eV above the valence band maximum for the FE phase. (b) plot in the $k_x = 0$ plane at the constant energy surface $E - E_{\text{VBM}} = 1.75$ eV for the AFE phase. (c) and (d) are zoomed-in views of panels (a) and (b) around the Γ point.

the spin-texture of the AFE phase can be approximated as $k_y\tau_y - k_z\tau_z$, displaying a Weyl character as predicted by the symmetry analysis.

The observed differences in the band structure and, even more, in the spin texture between the two phases reveal a particularly interesting effect. Since the FE and AFE phases are energetically competitive, it might be possible to explore means to stabilize one phase over the other, thereby tuning the effective spin-charge coupling and, consequently, the spintronic properties of the material. In the AFE phase, in particular, the Weyl-like spin texture is expected to give rise to the so-called "unconventional" current-induced spin polarization [76, 77, 78], where a charge current induces spin polarization of the conduction electrons along the current direction. This phenomenon, recently reported in Te, has drawn significant attention for the design of spintronic devices [76]. In SbSI, it can be further combined with the BPVE, investigated in the following, resulting in the integration of multiple functionalities.

3.4 Bulk photovoltaic effect

A photocurrent density \mathbf{j} driven by an electric field $\mathbf{E}(\omega)$ of frequency ω in the non-magnetic material SbSI can be written as [9, 12]

$$j^a = 2 \sum_{bc} \sigma^{abc}(\omega) \text{Re}[E^b(\omega)E^c(-\omega)] + t \sum_{bc} \eta^{abc}(\omega) \text{Im}[E^b(\omega)E^c(-\omega)] \quad (1)$$

where the first term represents the shift current (linear photogalvanic effect) and the second term corresponds to the injection current (circular photogalvanic effect). Both currents are expected to appear in both the FE and AFE phases, due to their non-centrosymmetric space groups, and more specifically, to their gyrotropy. $\sigma^{abc}(\omega)$ denotes a component of the shift photoconductivity tensor, which is real, while $\eta^{abc}(\omega)$ denotes a component of the circular injection photoconductivity tensor, which is imaginary. They are defined in the SI following Refs. [11, 12]. The indices a, b , and c label vector and tensor components; in particular, a indicates the direction of the photocurrent. t represents the electron relaxation time. The shift current corresponds to the dc part of the second-order response to the dipole electric field of light. In contrast, the injection photoconductivity corresponds to the rate of change of the interband dc part of the second-order response.

The photoconductivity tensors presented in the following are all computed starting from a Wannier interpolation of the GGA band structure calculated with SOC, as detailed in the Methods section and in the SI. The results obtained from the HSE band structure are very similar to the GGA ones, except for the position of the photoconductivity onset energy, which is shifted due to the (roughly rigid) upward shift of the conduction bands and related increase of the band gap. Due to this uncertainty on the band gap size, in the following, we will present all the results with the onset energy aligned with the experimental band gap value, as for common practice in the literature [11]. Since the value of the band gap in the AFE phase is similar to that in the FE phase, we shift the photocurrents in AFE configuration by the same amount.

3.4.1 Linear photovoltaic effect

In the FE phase, the shift photoconductivity tensor of SbSI has five independent non-zero components, namely σ^{zzz} , σ^{zxx} , σ^{zyy} , σ^{xxz} and σ^{yyz} , as allowed by the system's space group, Pna2₁. They are displayed in Fig. 5(a) as a function of the energy. All

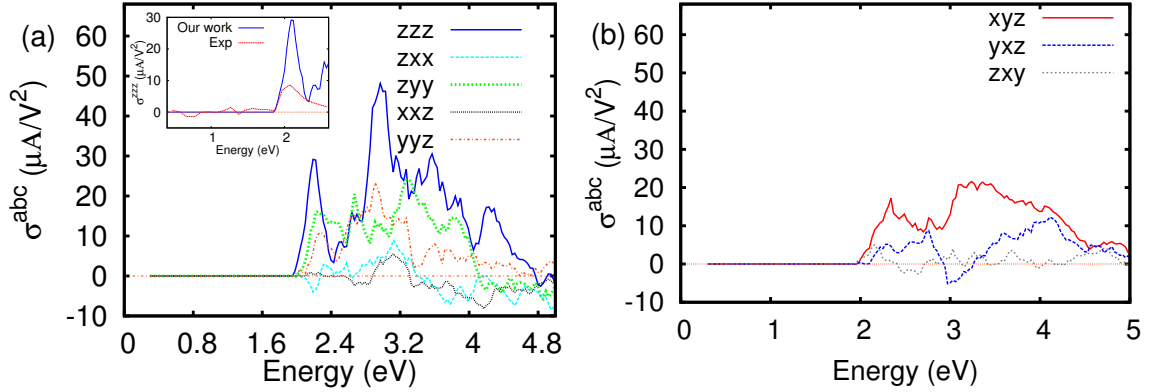


Figure 5: Non-zero independent components of shift photoconductivity tensor for the FE phase (a) and the AFE phase (b). The inset shows a comparison between our result for the σ^{zzz} and the experimental data from Ref. [50].

other components can be obtained from these independent components by exchanging the last two indices, related to the light polarization. The largest component is σ^{zzz} , corresponding to the electric field being polarized along the c axis and the current flowing in the same direction. The shift current is thus larger when the incident light is parallel to the FE distortion direction compared to the case when it is perpendicular. In the visible energy region ($E \sim 1.6 - 3.3$ eV), σ^{zzz} displays two prominent peaks, reaching about $30 \mu\text{A}/\text{V}^2$ at 2 eV and $47 \mu\text{A}/\text{V}^2$ at 3 eV. These peak values are significantly higher than those for prototypical FE compounds, like for BiFeO_3 and BaTiO_3 , where the maximum photoconductivities in the visible energy range are $0.05 \mu\text{A}/\text{V}^2$ and $5 \mu\text{A}/\text{V}^2$, respectively [30]. Hence, SbSI is potentially an excellent material candidate for bulk photovoltaic conversion.

The calculated σ^{zzz} can be compared to the experimental data [50], as shown in the inset of Fig. 5(a). While the shape of the first peak is qualitatively well reproduced, the experimentally measured maximum is significantly lower than the predicted one. Such discrepancies between measured and calculated shift photoconductivities have been reported in other studies on different materials. They are often attributed to the presence of multiple ferroelectric domains with opposite spontaneous polarizations in the sample, which reduces the overall shift current by averaging out the contributions from individual domains [38].

When transitioning to the AFE phase, the shift photoconductivity tensor is found to change compared to the FE case acquiring different non-zero components, as a result of the change in the crystal space group (see SI). Specifically, the independent components become σ^{xyz} , σ^{yxz} and σ^{zxy} . They are displayed in Fig. 5(b). The largest one is σ^{xyz} . Thus, the shift current in the AFE phase is expected to be maximized in the x direction, which is perpendicular to the chains, conversely to what is predicted in the FE phase. σ^{xyz} presents peaks of approximately $17 \mu\text{A}/\text{V}^2$ near 2 eV and $20 \mu\text{A}/\text{V}^2$ at 3 eV. These photoconductivity values are lower than those in the FE phase at similar energies, but still large if compared to the response of the prototypical bulk FE oxides [30].

To our knowledge, the shift current in the AFE phase has not been measured. Therefore, we lack benchmark experimental results for comparison. However, since the AFE

phase exists near room temperature, it should be experimentally accessible. Moreover, given that the non-zero components of the shift photoconductivity tensor differ between the FE and AFE phases, we suggest that measuring the shift conductivity could serve as a method to determine the phase of the material and follow the phase transition.

3.4.2 One-chain system

The maximum shift photoconductivity can be further enhanced by moving from bulk 3D materials to low-dimensional systems. For example, very large photoconductivities were predicted in two-dimensional ferroelectrics [36], like monolayer GeS and GeSe, and were related to the presence of van Hove singularities in the materials density of states (DOS) [34, 36]. In the case of SbSI, we can explore a similar idea by considering the extreme limit of one isolated chain, thus reducing the material to 1D.

The one-chain system is modelled considering the FE unit cell, removing one of the two chains, and increasing the lattice parameters along the transverse directions to $a = b = 12$ Å, to avoid interaction between periodically repeated images. Then, following Refs. [11, 36], the shift photoconductivity tensor components for the single chain σ_{SC}^{abc} are estimated by rescaling the results from the 3D supercell as $\sigma_{SC}^{abc} = \frac{a}{w_x} \frac{b}{w_y} \sigma^{abc}$ where w_a and w_b are the widths of the chain along the x and y directions, taken approximately equal to 2.62 Å and 6.57 Å (see SI).

The results for the one-chain system are displayed in Fig. 6, where only the components σ^{zzz} and σ^{zyy} are non-zero. In particular, σ^{zzz} reaches peak values one order of magnitude larger than those for the bulk systems, especially in the energy range between 2.5 and 3.2 eV. The shape of the spectrum is characterized by sharp peaks which can be clearly related to the van Hove singularities in the DOS, shown in the SI. This confirms the significant role these singularities play in enhancing the shift photoconductivity, similar to what has been reported in monolayer ferroelectrics.

Although isolating a single chain in experiments is challenging, it may be possible to fabricate nanowires with diameters of several nanometers, consisting of a few chains. This approach has already been demonstrated in tellurium, a material similarly composed of weakly van der Waals-bonded chains [76]. Nanowires of SbSI could exhibit photoconductivities that are intermediate between those of bulk and single-chain systems, thus offering exceptionally high photovoltaic performance.

3.4.3 Circular photogalvanic effect

In the FE state, the circular injection photoconductivity tensor has two independent components, namely η^{xxz} and η^{yyz} , allowed by symmetry. All other non-zero components are obtained from these by exchanging the last two indices and reversing the sign (see SI). Among these two independent components, η^{yyz} is considerably larger than η^{xxz} in the visible light energy range. It presents a first small peak of approximately 4×10^8 A/V²s at around 2.1 eV, followed by a significantly larger peak of 14×10^8 A/V²s at around 2.4 eV, and a sharp negative peak reaching -19×10^8 A/V²s at about 2.8 eV. As the energy increases, further large peaks are observed with the absolute value of the photoconductivity remaining quite large even outside the visible range.

It is particularly important to note that all η^{zbc} components in bulk FE SbSI are zero (for any a and b indices), indicating that the circular injection current is absent along the chains, but can only emerge in the transverse x and y directions, regardless of the light polarization. Interestingly, although the electronic bands are relatively flat in

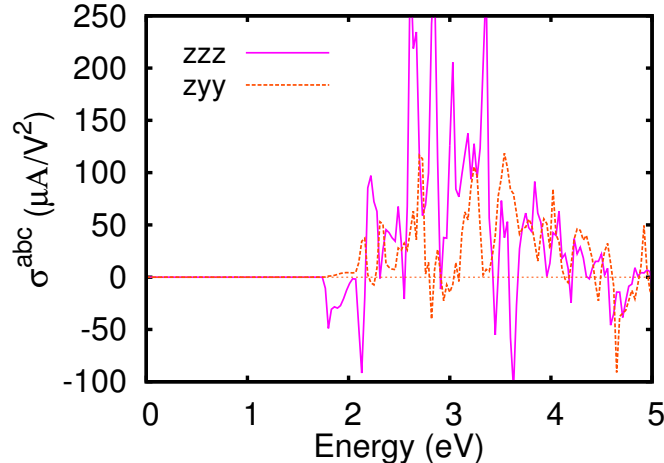


Figure 6: Non-zero components of the shift photoconductivity tensor for the one-chain system.

these perpendicular directions (i.e. the electron group velocity is quite small) owing to the weak inter-chain hybridization, the obtained photoconductivity peak values are an order of magnitude higher than those reported in other bulk materials, such as CdSe, CdS [26, 79, 80] and TaIrTe₄ [12], which have been recently studied by DFT calculations. This indicates that simple arguments based on qualitative inspections of the band structure do not always hold in the analysis of photocurrents. Accurate quantum mechanical calculations are generally required to obtain reliable predictions.

Turning to the AFE phase, we find that the independent components of the circular injection photoconductivity become η^{xyz} , η^{yxz} and η^{zxy} . Thus, at variance with what happens in the FE phase, the circular injection current can be measured along all directions, including along the chains (longitudinal direction), for an opportune choice of the light polarization.

The important result that the circular photogalvanic effect generates only transverse photocurrents in the FE phase, but also longitudinal photocurrents in the AFM phase, can be further confirmed through an alternative analysis. Specifically, by employing a distinct yet fully equivalent definition to Eq. (1), the circular photogalvanic effect is often characterized using a rank-two pseudotensor with components γ_{ab} [74], derived from the circular injection photoconductivity as $\gamma_{ab} \propto -i\epsilon_{bcd}\eta^{acd}$ (note the convention that repeated indices are summed over) [81]. This so-called circular photogalvanic pseudotensor has the same structure as the optical activity tensor, and its components transform like any other quantities that can be expressed as components of a rank-two pseudotensor [82]. These include the effective SOC terms introduced in section 3.3, such that a non-zero α_{ab} parameter must correspond a non-zero γ_{ab} . In other words, we can also predict the character of the circular photogalvanic effect by analyzing the spin texture, and vice versa [74]. In the case of FE SbSI, we find that the only two non-zero components of the circular photogalvanic pseudotensor are γ_{xy} and γ_{yx} , consistent with the non-zero spin-momentum coupling parameters α_{xy} and α_{yx} , describing the Rashba-Dresselhaus in-plane spin-texture in the band structure. In contrast, in the AFE phase, there are three non-zero and independent components, γ_{xx} , γ_{yy} , and moreover, γ_{zz} , which accounts for the longitudinal photocurrent. These components correspond to the effective spin-momentum coupling parameters α_{xx} , α_{yy} , and α_{zz} identified in the band structure analysis and are

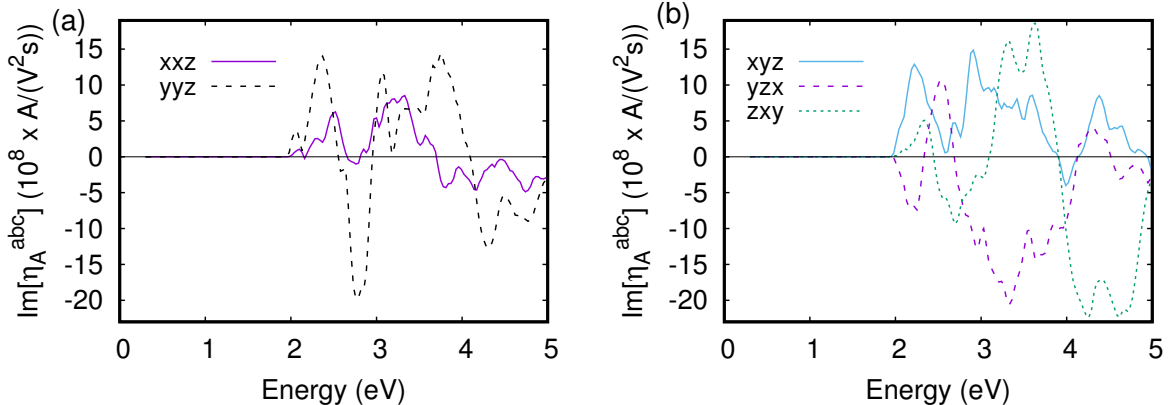


Figure 7: Non-zero independent components of the circular injection photoconductivity tensor for (a) the FE phase, and (b) the AFE phase.

consistent with the Weyl-Dresselhaus spin-texture.

In summary, our results show that the circular photovoltaic effect can be used to probe the FE-AFE transition in the same way as the linear photovoltaic effect since the non-zero components of the photoconductivity change with the phase symmetry. However, measuring the circular injection currents can provide additional information about spin-dependent properties of the material. This feature may eventually be important for the integration of the BPVE with spintronic functionalities.

4 Conclusions

In this paper, we presented a comprehensive investigation of the structural, electronic, and photoconductive properties of SbSI from first-principles, with particular attention to both the linear and circular photogalvanic contributions to the BPVE. Unlike previous studies, we centered our analysis on a comparison between the FE and the AFE phases.

We reproduced the crystal structures of the AFE and FE phases by using a hybrid functional approach combined with a van der Waals dispersion energy-correction term, which accounts for the weak interaction among the quasi-1D chains propagating along the c axis. We found that, although the FE phase had a lower energy, the AFE phase was close in energy and therefore competitive. In the FE phase, the atoms of the two chains of the unit cell move in the same direction along the c -axis and a net polarization appears due to the shift of the cation sub-lattice with respect to the anion one. In contrast, in the AFE phase the cations of different chains move in opposite directions along c , leading to a different space group and to a zero net polarization.

The phase transition is accompanied by a modification in the band structure. While the size of the band gap and the positions of the valence band maximum and conduction band minimum in the Brillouin zone remain essentially unchanged, the spin-texture transforms from Rashba-Dresselhaus in the FE phase to Dresselhaus-Weyl in the AFE phase. Notably, the latter case is expected to give rise to “unconventional” current-induced spin polarization, a phenomenon of interest for the design of spintronic devices.

To explore the BPVE, the shift and the circular injection photoconductivity tensors were calculated in both phases, yielding different non-zero independent components in each phase, consistent with their distinct space groups. Physically, this implies that the direction of the photocurrent can change during the FE-AFE transition, providing

a clear signature of the phase. Hence, we propose that the BPVE can serve as a reliable probe of the phase. Furthermore, we also showed that measuring the circular injection currents could access the spin-texture of the material, tracking its evolution from a Rashba-Dresselhaus to a Dresselhaus-Weyl character, and therefore, revealing the intricate coupling between structural and spintronic properties.

Finally, we predict that the shift photoconductivity of SbSI in the visible energy region is significantly larger than in most prototypical ferroelectric compounds, for both the FE and AFE phases. This finding confirms the potential of the material for photoconversion and photovoltaic applications.

Acknowledgements

The authors acknowledge Julen Ibañez Azpiroz and Alvaro Ruiz Puente for their technical support in the calculation of the photoconductivities. This work was supported by the Next-Generation-EU program via the PRIN-2022 SORBET 1133 (Grant No. 2022ZY8HJY), the ICSC initiative (National Center for High-Performance Supercomputing, 1134 Big Data and Quantum Computing), the PE4 Partenariato Quantum Science and Technology (NQSTI). High-performance computing resources and support were provided by the CINECA under the ISCRA IsB28 “HEXTIM”, IsCc2 ”SFERA” and IsCa7 ”MUSCHI2D” projects.

References

- [1] Zhenbang Dai and Andrew M. Rappe. Recent progress in the theory of bulk photovoltaic effect. *Chemical Physics Reviews*, 4(1):011303, 01 2023.
- [2] V. M. Fridkin. Bulk photovoltaic effect in noncentrosymmetric crystals. *Crystallography Reports*, 46(4):654, 2001.
- [3] Ralph von Baltz and Wolfgang Kraut. Theory of the bulk photovoltaic effect in pure crystals. *Phys. Rev. B*, 23:5590–5596, May 1981.
- [4] J. E. Sipe and A. I. Shkrebtii. Second-order optical response in semiconductors. *Phys. Rev. B*, 61:5337–5352, Feb 2000.
- [5] W. Shockley. *Electrons and Holes in Semiconductors*. D. Van Nostrand Company, Inc., New York, 1950.
- [6] Jonathan E. Spanier, Vladimir M. Fridkin, Andrew M. Rappe, Andrew R. Akbashev, Alessia Polemi, Yubo Qi, Zongquan Gu, Steve M. Young, Christopher J. Hawley, Dominic Imbrenda, Geoffrey Xiao, Andrew L. Bennett-Jackson, and Craig L. Johnson. Power conversion efficiency exceeding the shockley–queisser limit in a ferroelectric insulator. *Nature Photonics*, 10:611–616, 2016.
- [7] Qiong Ma, Roshan Krishna Kumar, Su-Yang Xu, Frank H. L. Koppens, and Justin C. W. Song. Photocurrent as a multiphysics diagnostic of quantum materials. *Nature Reviews Physics*, 5:170–184, 2023.
- [8] Junyeong Ahn, Guang-Yu Guo, and Naoto Nagaosa. Low-frequency divergence and quantum geometry of the bulk photovoltaic effect in topological semimetals. *Phys. Rev. X*, 10:041041, Nov 2020.

- [9] Hua Wang and Xiaofeng Qian. Electrically and magnetically switchable nonlinear photocurrent in pt-symmetric magnetic topological quantum materials. *npj Computational Materials*, 6, 2020.
- [10] Petr Král. Quantum kinetic theory of shift-current electron pumping in semiconductors. *Journal of Physics: Condensed Matter*, 12(22):4851, jun 2000.
- [11] Julen Ibañez Azpiroz, Stepan S. Tsirkin, and Ivo Souza. Ab initio calculation of the shift photocurrent by wannier interpolation. *Phys. Rev. B*, 97:245143, Jun 2018.
- [12] Álvaro R. Puente-Uribe, Stepan S. Tsirkin, Ivo Souza, and Julen Ibañez Azpiroz. Ab initio study of the nonlinear optical properties and dc photocurrent of the weyl semimetal tairte₄. *Phys. Rev. B*, 107:205204, May 2023.
- [13] Yang Zhang, Tobias Holder, Hiroaki Ishizuka, Fernando de Juan, Naoto Nagaosa, Claudia Felser, and Binghai Yan. Switchable magnetic bulk photovoltaic effect in the two-dimensional magnet cri₃. *Nature Communications*, 10(1):3783, Aug 2019.
- [14] Zhenbang Dai, Aaron M. Schankler, Lingyuan Gao, Liang Z. Tan, and Andrew M. Rappe. Phonon-assisted ballistic current from first-principles calculations. *Phys. Rev. Lett.*, 126:177403, Apr 2021.
- [15] D. H. Auston, A. M. Glass, and A. A. Ballman. Optical rectification by impurities in polar crystals. *Phys. Rev. Lett.*, 28:897–900, Apr 1972.
- [16] V. M. Asnin, A. A. Bakun, A. M. Danishevskii, E. L. Ivchenko, G. E. Pikus, and A. A. Rogachev. Observation of a photo-emf that depends on the sign of the circular polarization of the light. *JETP Letters*, 28:80, 1978.
- [17] D. Côté, N. Laman, and H. M. van Driel. Rectification and shift currents in GaAs. *Applied Physics Letters*, 80(6):905–907, 02 2002.
- [18] J. W. McIver, D. Hsieh, H. Steinberg, P. Jarillo-Herrero, and N. Gedik. Control over topological insulator photocurrents with light polarization. *Nature Nanotechnology*, 7(2):96–100, Feb 2012.
- [19] M. Nakamura, S. Horiuchi, F. Kagawa, N. Ogawa, T. Kurumaji, Y. Tokura, and M. Kawasaki. Shift current photovoltaic effect in a ferroelectric charge-transfer complex. *Nature Communications*, 8(1):281, Aug 2017.
- [20] Dylan Rees, Kaustuv Manna, Baozhu Lu, Takahiro Morimoto, Horst Borrmann, Claudia Felser, J. E. Moore, Darius H. Torchinsky, and J. Orenstein. Helicity-dependent photocurrents in the chiral weyl semimetal rhsi. *Science Advances*, 6(29):eaba0509, 2020.
- [21] Hongtao Yuan, Xinqiang Wang, Biao Lian, Haijun Zhang, Xianfa Fang, Bo Shen, Gang Xu, Yong Xu, Shou-Cheng Zhang, Harold Y. Hwang, and Yi Cui. Generation and electric control of spin–valley-coupled circular photogalvanic current in wse₂. *Nature Nanotechnology*, 9(10):851–857, Oct 2014.

- [22] Chang Niu, Shouyuan Huang, Neil Ghosh, Pukun Tan, Mingyi Wang, Wenzhuo Wu, Xianfan Xu, and Peide D. Ye. Tunable circular photogalvanic and photovoltaic effect in 2d tellurium with different chirality. *Nano Letters*, 23(8):3599–3606, 2023. PMID: 37057864.
- [23] M. D. Moldavskaya, L. E. Golub, S. N. Danilov, V. V. Bel’kov, D. Weiss, and S. D. Ganichev. Photocurrents in bulk tellurium. *Phys. Rev. B*, 108:235209, Dec 2023.
- [24] Noriyuki Urakami, Sho Ozaki, and Yoshio Hashimoto. Bulk photovoltaic effect of an alpha-phase indium selenide (α -In₂Se₃) crystal along the out-of-plane direction. *Applied Physics Letters*, 125(7):073102, 08 2024.
- [25] E. L. Ivchenko and G. E. Pikus. New photogalvanic effect in gyrotropic crystals. *JETP Letters*, 27:640, 1978.
- [26] F. Nastos and J. E. Sipe. Optical rectification and current injection in unbiased semiconductors. *Phys. Rev. B*, 82:235204, Dec 2010.
- [27] Fernando de Juan, Adolfo G. Grushin, Takahiro Morimoto, and Joel E. Moore. Quantized circular photogalvanic effect in weyl semimetals. *Nature Communications*, 8(1):15995, Jul 2017.
- [28] Rajender Prasad Tiwari. Enhanced shift current bulk photovoltaic effect in ferroelectric rashba semiconductor α -gete: ab initio study from three- to two-dimensional van der waals layered structures. *Journal of Physics: Condensed Matter*, 34(43):435404, aug 2022.
- [29] W. T. H. Koch, R. Munser, W. Ruppel, and P. Würfel. Anomalous photovoltage in batio₃. *Ferroelectrics*, 13(1):305–307, 1976.
- [30] Steve M. Young and Andrew M. Rappe. First principles calculation of the shift current photovoltaic effect in ferroelectrics. *Phys. Rev. Lett.*, 109:116601, Sep 2012.
- [31] Steve M. Young, Fan Zheng, and Andrew M. Rappe. First-principles calculation of the bulk photovoltaic effect in bismuth ferrite. *Phys. Rev. Lett.*, 109:236601, Dec 2012.
- [32] Keith T. Butler, Jarvist M. Frost, and Aron Walsh. Ferroelectric materials for solar energy conversion: photoferroics revisited. *Energy Environ. Sci.*, 8:838–848, 2015.
- [33] Liang Z Tan, Fan Zheng, Steve M Young, Fenggong Wang, Shi Liu, and Andrew M Rappe. Shift current bulk photovoltaic effect in polar materials—hybrid and oxide perovskites and beyond. *npj Computational Materials*, 2, 2016.
- [34] Ashley M. Cook, Benjamin M. Fregoso, Fernando de Juan, Sinisa Coh, and Joel E. Moore. Design principles for shift current photovoltaics. *Nature Communications*, 8, 2017.
- [35] Thibaud Etienne, Edoardo Mosconi, and Filippo De Angelis. Dynamical origin of the rashba effect in organohalide lead perovskites: A key to suppressed carrier recombination in perovskite solar cells? *The Journal of Physical Chemistry Letters*, 7, 2016.

- [36] Tonatiuh Rangel, Benjamin M. Fregoso, Bernardo S. Mendoza, Takahiro Morimoto, Joel E. Moore, and Jeffrey B. Neaton. Large bulk photovoltaic effect and spontaneous polarization of single-layer monochalcogenides. *Phys. Rev. Lett.*, 119:067402, Aug 2017.
- [37] Suman Raj Panday, Salvador Barraza-Lopez, Tonatiuh Rangel, and Benjamin M. Fregoso. Injection current in ferroelectric group-iv monochalcogenide monolayers. *Phys. Rev. B*, 100:195305, Nov 2019.
- [38] Yih-Ren Chang, Ryo Nanae, Satsuki Kitamura, Tomonori Nishimura, Haonan Wang, Yubei Xiang, Keisuke Shinokita, Kazunari Matsuda, Takashi Taniguchi, Kenji Watanabe, and Kosuke Nagashio. Shift-current photovoltaics based on a non-centrosymmetric phase in in-plane ferroelectric sns. *Advanced Materials*, 35(29):2301172, 2023.
- [39] Ryo Nanae, Satsuki Kitamura, Yih-Ren Chang, Kaito Kanahashi, Tomonori Nishimura, Redhwan Moqbel, Kung-Hsuan Lin, Mina Maruyama, Yanlin Gao, Susumu Okada, Kai Qi, Jui-Han Fu, Vincent Tung, Takashi Taniguchi, Kenji Watanabe, and Kosuke Nagashio. Bulk photovoltaic effect in single ferroelectric domain of sns crystal and control of local polarization by strain. *Advanced Functional Materials*, 34(41):2406140, 2024.
- [40] O. M. Madelung. *Semiconductors: Data Handbook*. Springer, Berlin, 2004.
- [41] Domenico Di Sante, Paolo Barone, Riccardo Bertacco, and Silvia Picozzi. Electric control of the giant rashba effect in bulk gete. *Advanced Materials*, 25(4):509–513, 2013.
- [42] Silvia Picozzi. Ferroelectric rashba semiconductors as a novel class of multifunctional materials. *Frontiers in Physics*, 2, 2014.
- [43] Sara Varotto, Luca Nessi, Stefano Cecchi, Jagoda Sławińska, Paul Noël, Simone Petró, Federico Fagiani, Alessandro Novati, Matteo Cantoni, Daniela Petti, Edoardo Albisetti, Marcio Costa, Raffaella Calarco, Marco Buongiorno Nardelli, Manuel Bibes, Silvia Picozzi, Jean-Philippe Attané, Laurent Vila, Riccardo Bertacco, and Christian Rinaldi. Room-temperature ferroelectric switching of spin-to-charge conversion in germanium telluride. *Nature Electronics*, 4(10):740–747, Oct 2021.
- [44] Fan Zheng, Liang Z. Tan, Shi Liu, and Andrew M. Rappe. Rashba spin-orbit coupling enhanced carrier lifetime in ch₃nh₃pb₃i₃. *Nano Letters*, 15(12):7794–7800, 2015. PMID: 26461166.
- [45] Pooya Azarhoosh, Scott McKechnie, Jarvist M. Frost, Aron Walsh, and Mark van Schilfhaarde. Research Update: Relativistic origin of slow electron-hole recombination in hybrid halide perovskite solar cells. *APL Materials*, 4(9):091501, 07 2016.
- [46] E. Fatuzzo, G. Harbeke, W. J. Merz, R. Nitsche, H. Roetschi, and W. Ruppel. Ferroelectricity in sb₂si. *Phys. Rev.*, 127:2036–2037, Sep 1962.
- [47] R. Nitsche and W.J. Merz. Photoconduction in ternary v-vi-vii compounds. *Journal of Physics and Chemistry of Solids*, 13(1):154–155, 1960.

- [48] Günther Harbeke. Absorption edge in ferroelectric sbisi under electric fields. *Journal of Physics and Chemistry of Solids*, 24(7):957–963, 1963.
- [49] N. Ogawa, M. Sotome, Y. Kaneko, M. Ogino, and Y. Tokura. Shift current in the ferroelectric semiconductor sbisi. *Phys. Rev. B*, 96:241203, Dec 2017.
- [50] Sotome M, Nakamura M, Fujioka J, Ogino M, Kaneko Y, Morimoto T, Zhang Y, Kawasaki M, Nagaosa N, Tokura Y, and Ogawa N. Spectral dynamics of shift current in ferroelectric semiconductor SbSI. *Proc Natl Acad Sci U S A*, 5(116):1929–1933, 2019.
- [51] Krystian Mistewicz, Marian Nowak, and Danuta Stróż. A ferroelectric-photovoltaic effect in sbisi nanowires. *Nanomaterials*, 9(4), 2019.
- [52] G. Kresse and J. Hafner. Ab initio molecular dynamics for liquid metals. *Phys. Rev. B*, 47:558–561, Jan 1993.
- [53] G. Kresse and J. Furthmüller. Efficiency of ab-initio total energy calculations for metals and semiconductors using a plane-wave basis set. *Computational Materials Science*, 6(1):15–50, 1996.
- [54] G. Kresse and J. Furthmüller. Efficient iterative schemes for ab initio total-energy calculations using a plane-wave basis set. *Phys. Rev. B*, 54:11169–11186, Oct 1996.
- [55] John P. Perdew, Kieron Burke, and Matthias Ernzerhof. Generalized gradient approximation made simple. *Phys. Rev. Lett.*, 77:3865–3868, Oct 1996.
- [56] Aliaksandr V. Krukau, Oleg A. Vydrov, Artur F. Izmaylov, and Gustavo E. Scuseria. Influence of the exchange screening parameter on the performance of screened hybrid functionals. *The Journal of Chemical Physics*, 125(22):224106, 12 2006.
- [57] J. Paier, M. Marsman, K. Hummer, G. Kresse, I. C. Gerber, and J. G. Ángyán. Screened hybrid density functionals applied to solids. *J. Chem. Phys.*, 124(15):154709, 2006.
- [58] S. Grimme, J. Antony, S. Ehrlich, and H. Krieg. A consistent and accurate ab initio parametrization of density functional dispersion correction (DFT-D) for the 94 elements H-Pu. *The Journal of Chemical Physics*, 132(15):154104, 04 2010.
- [59] R. D. King-Smith and David Vanderbilt. Theory of polarization of crystalline solids. *Phys. Rev. B*, 47:1651–1654, Jan 1993.
- [60] Nicola Marzari and David Vanderbilt. Maximally localized generalized wannier functions for composite energy bands. *Phys. Rev. B*, 56:12847–12865, Nov 1997.
- [61] Arash A. Mostofi, Jonathan R. Yates, Young-Su Lee, Ivo Souza, David Vanderbilt, and Nicola Marzari. wannier90: A tool for obtaining maximally-localised wannier functions. *Computer Physics Communications*, 178(9):685–699, 2008.
- [62] Giovanni Pizzi, Valerio Vitale, Ryotaro Arita, Stefan Blügel, Frank Freimuth, Guillaume Géranton, Marco Gibertini, Dominik Gresch, Charles Johnson, Takashi Kotetsune, Julen Ibañez-Azpiroz, Hyungjun Lee, Jae-Mo Lihm, Daniel Marchand, Antimo Marrazzo, Yuriy Mokrousov, Jamal I Mustafa, Yoshiro Nohara, Yusuke Nomura, Lorenzo Paulatto, Samuel Poncé, Thomas Ponweiser, Junfeng Qiao, Florian

- Thöle, Stepan S Tsirkin, Małgorzata Wierzbowska, Nicola Marzari, David Vanderbilt, Ivo Souza, Arash A Mostofi, and Jonathan R Yates. Wannier90 as a community code: new features and applications. *Journal of Physics: Condensed Matter*, 32(16):165902, jan 2020.
- [63] Jonathan R. Yates, Xinjie Wang, David Vanderbilt, and Ivo Souza. Spectral and fermi surface properties from wannier interpolation. *Phys. Rev. B*, 75:195121, May 2007.
- [64] Atsushi Kikuchi, Yoshio Oka, and Etsuro Sawaguchi. Crystal structure determination of sb₂si. *Journal of the Physical Society of Japan*, 23(2):337–354, 1967.
- [65] Danila Amoroso and Silvia Picozzi. Ab initio approach to structural, electronic, and ferroelectric properties of antimony sulphoiodide. *Phys. Rev. B*, 93:214106, Jun 2016.
- [66] C. Franchini, G. Kresse, and R. Podloucky. Polaronic hole trapping in doped batio₃. *Phys. Rev. Lett.*, 102:256402, Jun 2009.
- [67] A. Droghetti, C. D. Pemmaraju, and S. Sanvito. Polaronic distortion and vacancy-induced magnetism in mgo. *Phys. Rev. B*, 81:092403, Mar 2010.
- [68] E. Donges. X-ray structural analysis of ferroelectric antimony-sulfobromide. *Z. Anorg. Allg. Chem.*, 263:112, 1950.
- [69] Yoshio Oka, Atsushi Kikuchi, Toshio Mori, and Etsuro Sawaguchi. Atomic parameters in ferroelectric sb₂si. *Journal of the Physical Society of Japan*, 21(2):405B–406, 1966.
- [70] Ph. Ghosez, J.-P. Michenaud, and X. Gonze. Dynamical atomic charges: The case of ABo₃ compounds. *Phys. Rev. B*, 58:6224–6240, Sep 1998.
- [71] Xavier Gonze and Changyol Lee. Dynamical matrices, born effective charges, dielectric permittivity tensors, and interatomic force constants from density-functional perturbation theory. *Phys. Rev. B*, 55:10355–10368, Apr 1997.
- [72] Nicola A. Spaldin. A beginner’s guide to the modern theory of polarization. *Journal of Solid State Chemistry*, 195:2–10, 2012. Polar Inorganic Materials: Design Strategies and Functional Properties.
- [73] Keith T. Butler, Scott McKechnie, Pooya Azarhoosh, Mark van Schilfgaarde, David O. Scanlon, and Aron Walsh. Quasi-particle electronic band structure and alignment of the V-VI-VII semiconductors SbSI, SbSBr, and SbSeI for solar cells. *Applied Physics Letters*, 108(11):112103, 03 2016.
- [74] Sergey D. Ganichev and Leonid E. Golub. Interplay of rashba/dresselhaus spin splittings probed by photogalvanic spectroscopy – a review. *physica status solidi (b)*, 251(9):1801–1823, 2014.
- [75] Carlos Mera Acosta, Linding Yuan, Gustavo M. Dalpian, and Alex Zunger. Different shapes of spin textures as a journey through the brillouin zone. *Phys. Rev. B*, 104:104408, Sep 2021.

- [76] Francesco Calavalle, Manuel Suárez-Rodríguez, Beatriz Martín-García, Annika Johansson, Diogo C. Vaz, Haozhe Yang, Igor V. Maznichenko, Sergey Ostanin, Aurelio Mateo-Alonso, Andrey Chuvilin, Ingrid Mertig, Marco Gobbi, Fèlix Casanova, and Luis E. Hueso. Gate-tuneable and chirality-dependent charge-to-spin conversion in tellurium nanowires. *Nature Materials*, 21(5):526–532, May 2022.
- [77] Arunesh Roy, Frank T. Cerasoli, Anooja Jayaraj, Karma Tenzin, Marco Buongiorno Nardelli, and Jagoda Sławińska. Long-range current-induced spin accumulation in chiral crystals. *npj Computational Materials*, 8(1):243, Nov 2022.
- [78] Reena Gupta and Andrea Droghetti. Current-induced spin polarization in chiral tellurium: A first-principles quantum transport study. *Phys. Rev. B*, 109:155141, Apr 2024.
- [79] N. Laman, A. I. Shkrebti, J. E. Sipe, and H. M. van Driel. Quantum interference control of currents in CdSe with a single optical beam. *Applied Physics Letters*, 75(17):2581–2583, 10 1999.
- [80] N. Laman, M. Bieler, and H. M. van Driel. Ultrafast shift and injection currents observed in wurtzite semiconductors via emitted terahertz radiation. *Journal of Applied Physics*, 98(10):103507, 11 2005.
- [81] Stepan S. Tsirkin, Pablo Aguado Puente, and Ivo Souza. Gyrotropic effects in trigonal tellurium studied from first principles. *Phys. Rev. B*, 97:035158, Jan 2018.
- [82] Andrea Droghetti, Ivan Rungger, Angel Rubio, and Ilya V. Tokatly. Spin-orbit induced equilibrium spin currents in materials. *Phys. Rev. B*, 105:024409, Jan 2022.
- [83] M-I. Aroyo, J. M. Perez-Mato, C. Capillas, E. Kroumova, S. Ivantchev, G. Madariaga, A. Kirov, and H. Wondratschek. Bilbao crystallographic server i: Databases and crystallographic computing programs. *Zeitschrift fuer Kristallographie*, 221:15–27, 2006.
- [84] M-I. Aroyo, A. Kirov, , C. Capillas, J. M. Perez-Mato, and H. Wondratschek. Bilbao crystallographic server ii: Representations of crystallographic point groups and space groups. *Acta Cryst.*, A 62:115–128, 2006.

Supporting Information

S1 Structural properties

Tab. S1 reports the lattice constants and the atomic Wyckoff positions optimized using the HSE functional and taking into account the inter-chain Van der Waals (vdW) dispersion energy by means of the DFT-D3 correction. These results are also compared with the corresponding experimental data.

There is an overall good agreement between the calculated and experimental results for the FE phase. In both the FE and AFE phases, the chains elongate along the c -axis compared to the PE phase. This displacement of the Sb ions plays a dominant role in driving the transition from the PE to both the FE and AFE phases, as discussed in the main text.

Table S1: Lattice constants and atomic positions of SbSI in the FE ($Pna2_1$ space group, 4a Wyckoff positions), AFE ($P2_12_12_1$ space group, 4a Wyckoff positions) and PE ($Pnam$ space group, 4c Wyckoff positions) phases optimized using the HSE functional combined with the DFT-D3 vdW correction and compared with the available experimental data. The atomic Wyckoff positions are indicated in fractional coordinates.

	FE HSE	FE Exp. [69]	AFE HSE	PE HSE
a(Å)	8.56	8.49[68] (8.52[69] para)	8.60	8.59
b(Å)	10.10	10.10[68] (10.13[69] para)	10.07	10.13
c(Å)	4.16	4.16[68] (4.10[69] para)	4.17	4.09
x_{Sb}	0.12	0.12	0.12	0.12
y_{Sb}	0.12	0.12	0.12	0.12
z_{Sb}	0.31	0.30	0.19	0.25
x_S	0.85	0.84	0.85	0.85
y_S	0.05	0.05	0.05	0.05
z_S	0.26	0.26	0.24	0.25
x_I	0.50	0.51	0.50	0.50
y_I	0.83	0.83	0.83	0.82
z_I	0.24	0.25	0.26	0.25

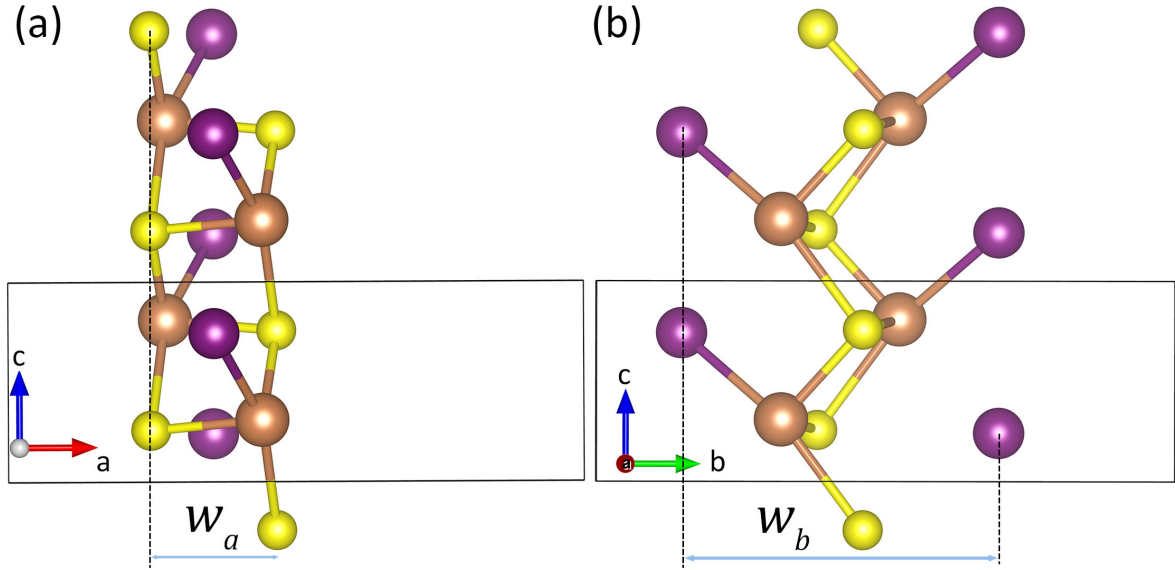


Figure S1: Supercell used to model the single-chain system. (a) a - c view, (b) b - c view. w_a and w_b are the widths of the chain along the x and y directions, respectively.

S2 Single-chain system

Fig. S1 displays the supercell used to model the single-chain system. w_a and w_b are the estimated widths of the chain in the x and y directions, which are used for the renormalization of the photoconductivity in the main text.

S3 Born effective charges (BEC)

Tables S2 and S3 report the BEC for the FE phase obtained within the GGA and using HSE, respectively. We see that the differences between the HSE and GGA results are overall negligible.

Table S4 presents the GGA BEC for the AFE phase.

	Z_{xx}^*	Z_{xy}^*	Z_{xz}^*	Z_{yx}^*	Z_{yy}^*	Z_{yz}^*	Z_{zx}^*	Z_{zy}^*	Z_{zz}^*
Sb	1.96	0.07	0.03	0.87	3.51	0.38	0.13	-0.12	5.97
S	-1.16	-0.10	-0.08	-0.85	-1.72	-0.09	-0.27	-0.40	-3.43
I	-0.80	-0.41	0.03	-0.78	-1.79	-0.17	-0.06	-0.23	-2.53

Table S2: Born effective charges of the FE phase calculated with the GGA.

	Z_{xx}^*	Z_{xy}^*	Z_{xz}^*	Z_{yx}^*	Z_{yy}^*	Z_{yz}^*	Z_{zx}^*	Z_{zy}^*	Z_{zz}^*
Sb	1.97	0.06	0.00	0.81	3.62	0.44	0.10	-0.07	6.10
S	-1.22	-0.12	-0.08	-0.85	-1.81	-0.08	-0.29	-0.37	-3.56
I	-0.75	-0.43	0.02	-0.79	-1.81	-0.20	-0.08	-0.25	-2.54

Table S3: Born effective charges of the FE phase calculated by using the HSE functional.

	Z_{xx}^*	Z_{xy}^*	Z_{xz}^*	Z_{yx}^*	Z_{yy}^*	Z_{yz}^*	Z_{zx}^*	Z_{zy}^*	Z_{zz}^*
Sb	1.89	0.10	0.04	0.85	3.52	-0.38	-0.13	0.18	6.03
S	-1.14	-0.11	0.10	-0.83	-1.71	0.07	0.28	0.39	-3.45
I	-0.75	-0.38	-0.15	-0.75	-1.81	-0.22	-0.24	-0.20	-2.57

Table S4: Born effective charges of AFE phase calculated with the GGA.

S4 Band structures

Fig. S2 displays the DFT band structure of the FE and AFE phases, alongside the Wannier bands. The DFT bands (red lines) are well reproduced by the Wannier bands (blue lines) in a wide energy range around the Fermi level, namely from -5 to 5 eV. In panel (a), the DFT band structure of the FE phase is obtained within the GGA. In panel (b), the DFT band structure of the FE phase is obtained using the HSE hybrid functional. HSE produces only a rigid shift of the conduction bands compared to GGA without modifying the main electronic features. In panel (c), the DFT band structure of the AFE phase is obtained within the GGA.

Fig. S3 shows the Wannier band structure for the single-chain system.

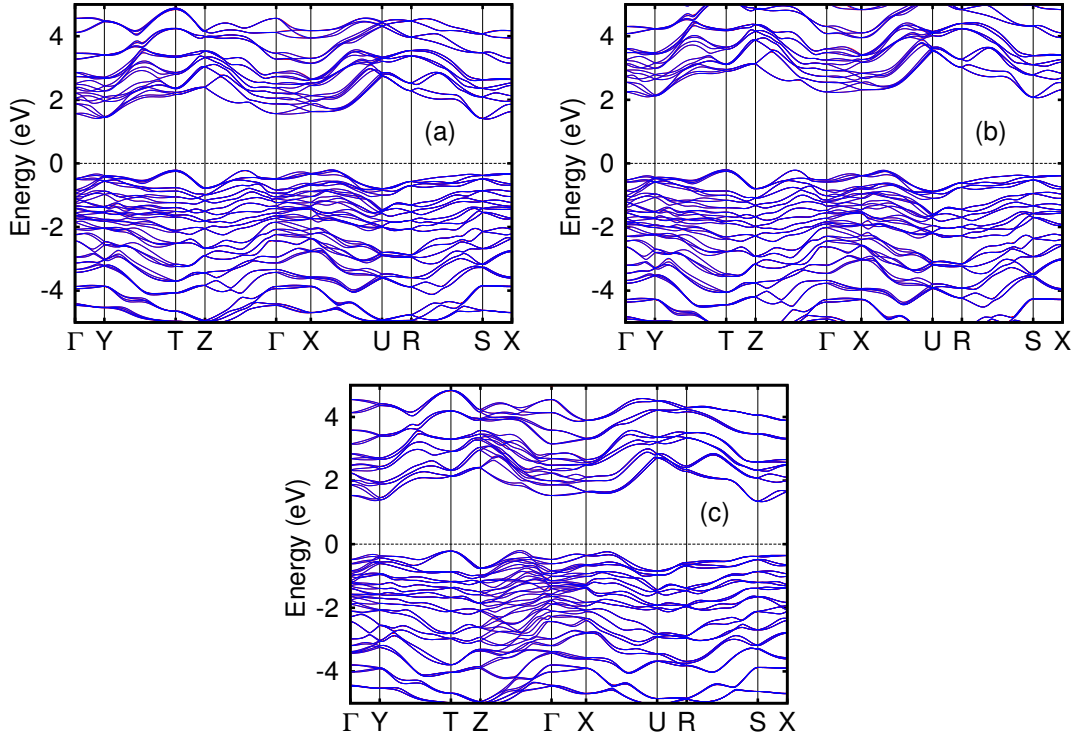


Figure S2: DFT band structure (red lines) and Wannier-interpolated band structures (blue lines). (a) DFT Band structure for the FE phase calculated within the GGA. (b) DFT band structure for the FE phase calculated using HSE. (c) DFT Band structure for the AFE phase calculated within the GGA. In all plots, the Fermi energy is set at 0 eV.

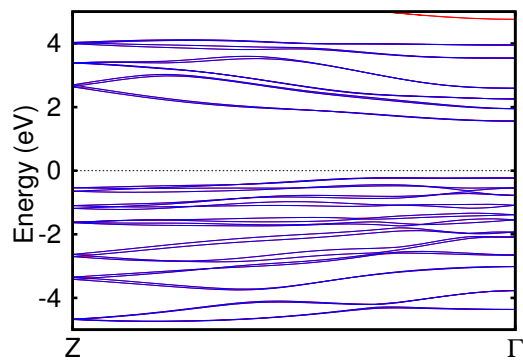


Figure S3: DFT band structure (red lines) and Wannier-interpolated band structure (blue lines) for the single-chain system. The Fermi energy is set at 0 eV.

S5 Density of states

Fig. S4(a) and (b) show the DOS of FE phase for the bulk and the single-chain systems, respectively. The results are obtained with the GGA. In the DOS of the single-chain system, we can clearly observe the appearance of van Hove singularities, which eventually will lead an enhancement of the photoconductivity, as described in the paper.

In addition to the DOS, we can also compute the joint density of states (JDOS). The JDOS quantifies the number of possible optical transitions between the occupied valence bands and the unoccupied conduction bands. It is defined as [11]

$$D_{joint} = \frac{V_c}{\hbar} \int_{BZ} \frac{d^3k}{(2\pi)^3} \sum_{n,m} f_{nm} \delta(\omega_{mn} - \omega), \quad (2)$$

where V_c is the cell volume, n and m label two Bloch states $|n\rangle$ and $|m\rangle$ of energy ϵ_n and ϵ_m , respectively. $f_{nm} = f_n - f_m$ is the difference between the Fermi occupation factors, and $\omega_{nm} = (\epsilon_n - \epsilon_m) / \hbar$ is the optical excitation frequency.

Figs. S4(c) and (d) present the the JDOS of FE phase for the bulk and the single-chain systems, respectively, as calculated within the GGA. The onset energy corresponds to the band gap size, which is nearly identical for both the bulk and single-chain systems. Like the DOS, the JDOS of the single chain also displays sharp peaks corresponding to van Hove singularities.

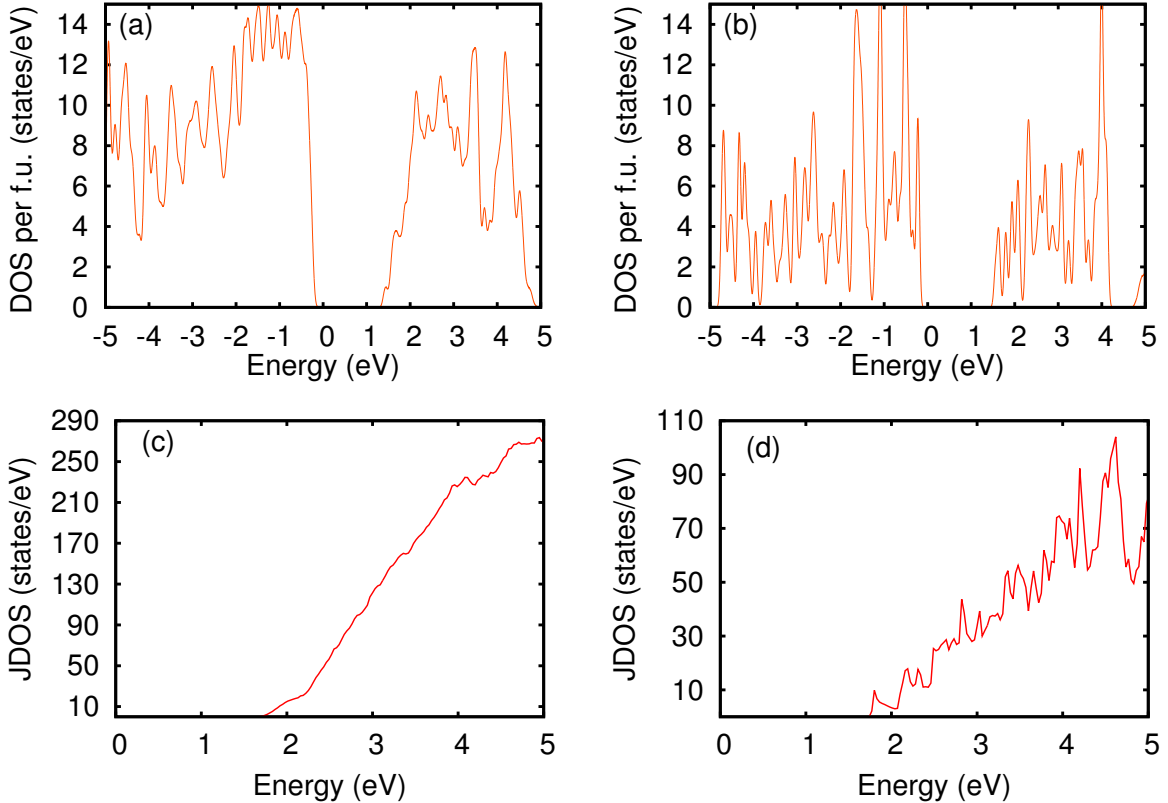


Figure S4: DOS of the FE phase for the bulk system (a) and the single-chain system (b). JDOS of the FE phase for the bulk system (c) and the single-chain system (d).

S6 Bulk photovoltaic effect

S6.1 Shift photoconductivity

The shift photoconductivity tensor is defined as [11]

$$\sigma^{abc} = -\frac{i\pi e^3}{4\hbar^2} \int_{BZ} \frac{d^3k}{(2\pi)^3} \sum_{n,m} f_{nm} [r_{mn}^b r_{nm;a}^c + (b \leftrightarrow c)] \times [\delta(\omega_{mn} + \omega) + \delta(\omega_{mn} - \omega)]. \quad (3)$$

In this equation, e is the electron charge and the other quantities are defined as above. Additionally, we have introduced the interband dipole matrix

$$r_{nm}^a = (1 - \delta_{nm}) A_{nm}^a, \quad (4)$$

and its derivative

$$r_{nm;b}^a = \partial_b r_{nm}^a - i(A_{nm}^b - A_{mn}^b) r_{nm}^a, \quad (5)$$

which depend on the Berry connection

$$A_{nm}^a = i \langle n | \partial_a | m \rangle, \quad (6)$$

with $\partial_a = \frac{\partial}{\partial k^a}$.

S6.2 Injection photoconductivity

The injection photoconductivity is defined as [12]

$$\eta^{abc} = -\frac{\pi e^3}{\hbar^2} \int_{BZ} \frac{d^3k}{(2\pi)^3} \sum_{n,m} f_{nm} \frac{\partial \omega_{mn}}{\partial k^a} r_{nm}^b r_{mn}^c \delta(\omega_{mn} - \omega), \quad (7)$$

which can be separated into a symmetric (S) and an antisymmetric (A) part under the exchange of indices $b \leftrightarrow c$:

$$\begin{aligned} \eta_S^{abc} &= \frac{1}{2} [\eta^{abc}(\omega) + \eta^{acb}(\omega)], \\ \eta_A^{abc} &= \frac{1}{2} [\eta^{abc}(\omega) - \eta^{acb}(\omega)]. \end{aligned}$$

η_S^{abc} and η_A^{abc} are real and imaginary, respectively. η_S^{abc} describes the response to a linearly polarized light, and vanishes in SbSI because of time-reversal symmetry. η_A^{abc} describes the response to a circularly polarized light. Since, in the paper and in the following, we only consider this antisymmetric part, we drop the subscript ‘‘A’’ to keep the notation lighter.

S6.3 Symmetry analysis for the photoconductivity tensors

Using the Bilbao Crystallographic Server (BCS) [83, 84], we can readily identify the non-zero and independent components of the shift and injection photoconductivity tensors based on the space group of our system.

S6.3.1 Shift photoconductivity

The shift photoconductivity is a rank-three polar tensor (i.e, even under time-reversal), symmetric with respect to the exchange of its last two indices. By relabeling the Cartesian directions x , y and z as 1, 2, 3, respectively, we adopt the BCS abbreviated notation and write its components as $\sigma^{abc} \rightarrow \sigma^{ab}$ where

$$bc \rightarrow \begin{cases} b & \text{if } b = c \\ 9 - (b + c) & \text{if } b \neq c \end{cases}.$$

The independent shift photoconductivity components can then be presented in a table with three rows and six columns, corresponding to the indices a and b , respectively.

For the FE phase (space group Pna2₁), we obtain

σ^{ab}	1	2	3	4	5	6
1	0	0	0	0	σ^{15}	0
2	0	0	0	σ^{24}	0	0
3	σ^{31}	σ^{32}	σ^{33}	0	0	0

where the non-zero components are $\sigma^{15} \rightarrow \sigma^{113} \equiv \sigma^{xxz}$, $\sigma^{24} \rightarrow \sigma^{223} \equiv \sigma^{yyz}$, $\sigma^{31} \rightarrow \sigma^{311} \equiv \sigma^{zxx}$, $\sigma^{32} \rightarrow \sigma^{322} \equiv \sigma^{zyy}$, and $\sigma^{33} \rightarrow \sigma^{333} \equiv \sigma^{zzz}$, as reported in the main text.

In contrast, for the AFE phase (space group P2₁2₁2₁), we obtain

	1	2	3	4	5	6
1	0	0	0	σ^{14}	0	0
2	0	0	0	0	σ^{25}	0
3	0	0	0	0	0	σ^{36}

where the non-zero components are $\sigma^{14} \rightarrow \sigma^{123} \equiv \sigma^{xyz}$, $\sigma^{25} \rightarrow \sigma^{213} \equiv \sigma^{yxz}$, and $\sigma^{36} \rightarrow \sigma^{312} \equiv \sigma^{zxy}$.

S6.3.2 Circular injection photoconductivity

The circular injection photoconductivity is a rank-three polar tensor (i.e, even under time-reversal), antisymmetric with respect to the exchange of its last two indices. Following the BCS, its components η^{abc} can be represented in a table with three rows, corresponding to the index a , and nine columns corresponding to the indices bc .

For the FE phase (space group Pna2₁), we obtain

η^{abc}	11	21	31	12	22	32	13	23	33
1	0	0	$-\eta^{113}$	0	0	0	η^{113}	0	0
2	0	0	0	0	0	$-\eta^{223}$	0	η^{223}	0
3	0	0	0	0	0	0	0	0	0

Thus, there are four non-zero components of the circular injection photoconductivity, but only two of them are independent, namely $\eta^{113} \equiv \eta^{xxz}$ and $\eta^{223} \equiv \eta^{yyz}$, as reported in the main text.

In the case of the AFE phase (space group P2₁2₁2₁), we obtain

η^{abc}	11	21	31	12	22	32	13	23	33
1	0	0	0	0	0	$-\eta^{123}$	0	η^{123}	0
2	0	0	$-\eta^{213}$	0	0	0	η^{213}	0	0
3	0	$-\eta^{312}$	0	η^{312}	0	0	0	0	0

We therefore find three independent components of the circular injection photoconductivity, that are $\eta^{123} \equiv \sigma^{xyz}$, $\eta^{213} \equiv \sigma^{yxz}$, and $\eta^{321} \equiv \sigma^{zxy}$.

S7 Photoconductivity: GGA versus HSE

Fig. S5 compares the σ^{zzz} component of the shift photoconductivity tensor for the FE phase calculated within the GGA and using HSE. Both plots are shifted to align the onset energies with the experimental band gap. We observe that the peak at about 3 eV is slightly reduced in the HSE result. Nonetheless, the differences between the two spectra are overall minor, reflecting the negligible differences in the band structure obtained with the two methods. Thus, we present only the GGA results in the main text.

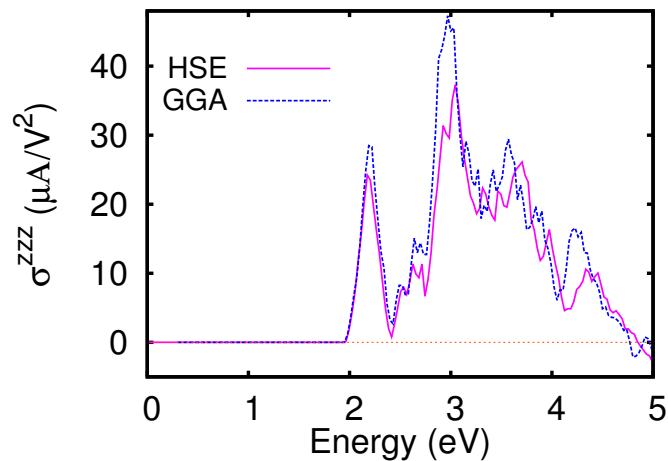


Figure S5: σ^{zzz} component of the shift photoconductivity tensor calculated within the GGA and using HSE.